Journal of
Materials Chemistry A
Materials for energy and sustainability

This article can be cited before page numbers have been issued, to do this please use: C. E. Chukwuneke, K. Kawashima, T. Nguyen, G. Ruiz, J. Smith, R. A. Marquez, J. T. Bender, J. L. Ng, X. Zhan, W. Wang, D. Milliron, M. Rose and C. Mullins, *J. Mater. Chem. A*, 2026, DOI: 10.1039/D5TA09289B.

ROYAL SOCIETY
OF CHEMISTRY

rsc.li/materials-a

View Article Online
DOI: 10.1039/D5TA09289B

ARTICLE

Cerium-Doping and Nitridation Effects on Nickel-based Metal Organic Framework for Alkaline Water Oxidation

Received 00th January 20xx,
Accepted 00th January 20xx

DOI: 10.1039/x0xx00000x

Chikaodili E. Chukwuneke[a,d], Kenta Kawashima[a], Tran Phuoc Anh Nguyen[a], Gabriella Ruiz[a], Johnpaul Smith[a], Raul A. Marquez[a], Jay T. Bender[b], Jing Lian Ng[b], Xun Zhan[b], Wennie Wang[b,c,d] Delia J. Milliron[a,b,c,d,e], Michael J. Rose[a,d], C. Buddie Mullins[a,b,c,d,e*]

In the quest for a green energy future, renewable energy-driven hydrogen production via alkaline water electrolyzers leads toward a sustainable human society. However, the complementary oxygen evolution reaction (OER) in alkaline water electrolysis limits the overall electrolyzer efficiency since it requires complex, multi-step electron transfer. This work introduces a synthetic strategy that translates a less-conductive Ce-doped nickel metal-organic framework (MOF) into a conductive precatalyst (i.e., a Ce-doped nickel nitride and carbon-based material composite) through nitrogen incorporation. The impact of nitrogen incorporation leads to the formation of a nitride phase, and a carbon-based material phase, while the Ce^{3+} species leads to the formation of pseudo-tetrahedral geometries on Ni sites, which enhances OER kinetics marked by a Tafel slope of 83.6 mV dec^{-1}. Nitridation led to approximately 50× improvement in OER activity relative to the parent MOFs. Moreover, the combined effect of cerium doping and nitridation produced a synergistic effect with $Ce_{0.03}Ni_{0.97}$-NMOF, achieving a Faradaic efficiency of 100% and maintaining stable operation for 24 hours at a current density of 10 mA cm^{-2}, exhibiting even higher activity after prolonged testing.

Introduction

Energy is essential for productive living on any planet in the "Milky Way", and as human technologies continue to advance, more of it is needed. Intermittent energy sources such as solar, wind, and hydropower offer opportunities but are faced with the downside of being occasionally intermittent. One of the ways of ensuring energy efficiency and curbing waste from sporadic fuel sources is by storing them in chemical bonds through energy conversion devices. In recent times, water-splitting technologies have been on the front burner to ensure a sustainable and green source of hydrogen production. For hydrogen production to be industrially efficient, catalyzing the oxygen evolution reaction (OER), a complementary reaction of the hydrogen production from water in an electrochemical cell, is essential to lower its overall energy requirement.

Electrocatalysts are employed to lower the energy requirement per product, and classes of materials such as metal-organic frameworks (MOFs) have been utilized owing to their superior high surface area, flexible structure, high porosity, and high tunability owing to the numerous possible combinations of ligands and metal salts.[1,2] Despite the promising catalytic properties MOFs possess, they have a major drawback of poor electron transport due to the insulating nature of the organic linkers and instability under OER conditions.[3–5] This challenge has inspired innovative approaches to transforming non-conductive MOFs into conductive precatalysts, which undergo in-situ transformation into metal oxide OER catalysts,[6,7] with improved electrical conductivity, while capitalizing on their advantages.[8]

In transforming the MOFs into better precatalysts, synthetic designs leading to derived metal nanoparticles,[9–14] oxides,[15–19] chalcogenides,[20–30] and phosphides[31–37] have been studied; however, nitrides have not been well studied. In fact, literature shows only one investigation of a MOF-derived nitride precatalyst[38] and a drawback to the extant synthetic strategy is the conductivity and surface area penalty associated with the carbon framework lost during the process.[11] Another technique for making MOF-derived precatalysts more active is cation doping (e.g., Ce), which has been demonstrated to help create active sites by modifying the material's electronic structure, leading to enhanced conductivity and stabilization of OER intermediates.[39–42]

Here, we outline a site engineering strategy by employing nitridation and doping techniques. In this study, we dope the parent Ni-MOF (called Ce_0Ni_1-MOF) with 1, 3, and 5% Ce doping ($Ce_{0.01}Ni_{0.99}$-MOF, $Ce_{0.03}Ni_{0.97}$-MOF, and $Ce_{0.05}Ni_{0.95}$-MOF, respectively) after which nitridation aided the formation of

---

[a] *Department of Chemistry, College of Natural Sciences, The University of Texas at Austin, Austin, Texas 78712, USA*
[b] *McKetta Department of Chemical Engineering, The University of Texas at Austin, Austin, Texas 78712, USA.*
[c] *Texas Materials Institute, The University of Texas at Austin, Austin, Texas 78712, USA*
[d] *Allen J. Bard Center for Electrochemistry, The University of Texas at Austin, Austin, Texas 78712, USA*
[e] *H2@UT, The University of Texas at Austin, Austin, Texas 78712, USA.*

Supplementary Information available: [details of any supplementary information available should be included here]. See DOI: 10.1039/x0xx00000x

View Article Online
DOI: 10.1039/D5TA09289B

nickel nitride species. We demonstrate that nitridation can selectively incorporate nitrogen into the lattice structure of nickel in a MOF structure while retaining the carbon framework. The resulting nickel nitride phase and carbon framework aided conductivity, while Ce-doping is hypothesized to create a pseudo-tetrahedral geometry on nickel sites, which aids the OER. We also provide a molecular structure hypothesizing the existence of a pseudo-tetrahedral geometry on the nickel sites due to Ce-doping, which, to the best of our knowledge, hasn't been reported for MOF-derived precatalysts for the OER. Our results show that the combined site design techniques improved the electrochemical activity of the precatalyst relative to the parent MOF

Experimental Methods

Materials

Nickel nitrate hexahydrate (99% purity, Thermo Scientific), cerium nitrate hexahydrate (99% purity, Sigma Aldrich), terephthalic acid (TPA) (98% purity, Sigma Aldrich), NaOH (97% purity, Sigma Aldrich), KOH (90% purity, Sigma Aldrich), isopropanol (99.5% purity, Sigma Aldrich), dimethylformamide (DMF) (99.8%, Fisher chemicals), and ammonia gas (Airgas) were used for electrode synthesis and electrochemical reactions.

Electrocatalyst Synthesis

Synthesis of Ni-MOF and Ce-doped Ni-MOF Precursors

Ni-MOF (called Ce_0Ni_1-MOF) was synthesized by following a modified method [43] in which 96 mg of $Ni(NO_3)_2$, 166 mg of TPA, and 20 mL of DMF were mixed. This was followed by the dropwise addition of 2 mL of 400 mM NaOH while stirring the mixture for 30 minutes. NaOH facilitates the deprotonation of the carboxylic acid groups in the organic linker and adjusts the solution pH, thereby enabling the coordination of Ni^{2+}/Ce^{3+} ions with terephthalate anions and promoting MOF crystallization. The Ce-doped Ni-MOF ($Ce_{0.01}Ni_{0.99}$-MOF, $Ce_{0.03}Ni_{0.97}$-MOF, and $Ce_{0.05}Ni_{0.95}$-MOF) were prepared on a Ni:Ce mole ratio basis and were prepared by following the same method as described in the synthesis of the bulk Ni-MOF with the addition of 1, 3, and 5 moles % Ce $(NO_3)_3 \cdot 6H_2O$. After the addition of Ce salt, DMF is added followed by stirring, and addition of 2 mL of 400 mM NaOH in that order before it is transferred to the reactor for the solvothermal reaction in the furnace. The furnace is ramped to 100 °C at 5°C/ minute and maintained at the final temperature for 8 h. After synthesis, the MOF is washed with DMF and ethanol, respectively, sequentially before centrifugation and allowed to dry overnight at 60 °C in a vacuum oven. The synthesis resulted in the pure Ni-MOF yield of ~92.4%.

Synthesis of MOF-derived Ni_3N and Ce-doped Ni_3N Precatalysts

The as-synthesized Ce_0Ni_1-MOF was converted into a composite of nickel nitride (Ni_3N) and carbon framework by flowing NH_3 gas over 100 mg of Ce_0Ni_1-MOF at a flow rate of 50 sccm at varying temperatures (300-450 °C) in a horizontal tube furnace to arrive at an optimized temperature of 350 °C. The Ce_0Ni_1-MOF was heated from room temperature to the optimized temperature at a ramp rate of 5 °C/min and held for another for 1h all under an ammonia ambient. During the cooling phase, when the temperature gets below 100 °C, the gas flow is switched from NH_3 to N_2 to maintain an inert environment, resulting in the formation of a MOF-derived Ni_3N electrocatalyst Similarly, the MOF-derived Ce-doped Ni_3N electrocatalysts ($Ce_{0.01}Ni_{0.99}$-NMOF, $Ce_{0.03}Ni_{0.97}$-NMOF, and $Ce_{0.05}Ni_{0.95}$-NMOF) were prepared by following the same method as described in the synthesis of the MOF-derived Ni_3N precatalyst but at the optimized temperature obtained from its synthesis. The synthesis resulted in the composite yield of 72.4%.

Characterization

The crystallinity of the resultant Ce_0Ni_1-MOF, Ce-doped Ni MOFs, and their corresponding nitrides were characterized with a Rigaku MiniFlex 600 X-ray diffractometer with Cu Kα radiation (λ = 1.54186 Å) source was used to obtain the X-ray diffraction patterns (XRD) of the materials. An Apreo 2 C LoVac scanning electron microscope (SEM) with a Bruker energy dispersive X-ray detector (EDX) was used to investigate the precatalysts' morphologies and bulk elemental composition. Surface compositions of the samples were evaluated using a PHI Versaprobe4 X-ray photoelectron spectrometer (XPS) with Mg Kα1 radiation (hv = 1253.7 eV). Fourier-transform infrared spectroscopy (FTIR) was used to evaluate the functional groups and were obtained using a InvenioR system. Transmission electron microscope (TEM) images were obtained using a JEOL NeoARM system. The 7500ce quadrupole inductively coupled plasma mass spectrometry (ICP-MS) was used to evaluate the metal content of the precatalyst.

Electrochemical Measurements

Electrochemical reactions were made using a CHI 608D potentiostat coupled to a three-electrode setup in a Teflon cell. The three-electrode setup consists of a graphite counter electrode, a Hg/HgO reference electrode (internal solution: 1 M KOH), the as-prepared loaded glassy carbon electrode as a working electrode, and 1 M KOH aqueous solution as an electrolyte. Here, the working electrode was prepared via a drop-casting method (catalyst loading amount: 0.3 mg cm^{-2}). The ink was prepared by dissolving 2.5 mg of the sample in 1 mL of ~ 0.05wt% Fumion (dissolved in isopropanol). To remove O_2 bubbles during the electrochemical tests, a rotating disk electrode (RDE, Pine Instrument) system was used (rotating speed: 1600 rpm). All measurements were converted from V vs Hg/HgO to V vs the reversible hydrogen electrode (RHE) using the Nernst equation:[44]

$$E_{\mathrm{RHE}} = E_{\mathrm{Hg/HgO}} + 0.0592 \times \mathrm{pH} + E^{\circ}_{\mathrm{Hg/HgO}}$$
$$E^{\circ}_{\mathrm{Hg/HgO}}(1\mathrm{M\ KOH}) = 0.1053\ \mathrm{V\ at\ 25°C}$$

The electrochemical behavior of the resultant nitride precatalysts was evaluated using the following electrochemical protocol. First, the precatalysts are activated using CV cycles at a scan rate of 5 mV s^{-1} until three consecutive replicate CVs are obtained. The three consecutive replicate CVs indicate that the

View Article Online
DOI: 10.1039/D5TA09289B

catalytic surface is stable. Immediately after the activation, electrochemical impedance spectroscopy (EIS) was utilized to obtain the uncompensated resistance (R_{u}) and the charge transfer resistance (R_{ct}) using an applied voltage of 0.70 V vs Hg/HgO. In addition, EIS was utilized in obtaining the double layer capacitance value (C_{dl}) by using the equation

$$C_{\mathrm{dl}} = CPE_{\mathrm{ct}} \times (\omega_{\max})^{n-1}$$

Where CPE_{ct} represents the charge transfer resistance of the constant phase element, $\omega_{\max}$ stands for the maximum frequency of the imaginary component of the Nyquist plot, and n defines the deviation from ideal capacitance.

Next, the surface of the electrocatalysts was completely oxidized using chronopotentiometry (CP) at a current density of 2.5 mA cm^{-2} for 10 minutes (see Figure S21) to ensure that the current response while measuring the Tafel slope can be ascribed to OER currents only. Subsequently, MUSCP was used to obtain the Tafel slope. MUSCP was executed using a constant current density from 0.5 to 3 mA cm^{-2} at an incremental value of 0.5 mA cm^{-2}. Twenty-four hours of long-term CP testing was done at a current density of 10 mA cm^{-2} using 2.5 mg of precatalyst dissolved in 0.2 wt.% Nafion® perfluorinated resin solution (dissolved in isopropanol) (Sigma Aldrich).

Faradaic Efficiency Measurements

Faradaic efficiency was measured using a Hoffman cell in which one of the arms serves as the collection point for the hydrogen evolution reaction (HER) and the other, the OER. The HER side was catalyzed by a standard Pt/C electrode, while the OER side was catalyzed by the precatalysts of interest, which are Ce_0Ni_1-NMOF and $Ce_{0.03}Ni_{0.97}$-NMOF drop-casted on a carbon paper. The Hoffman cell was filled appropriately with 1 M KOH, the HER side of the cell served as the counter electrode, while the OER side holding the tested precatalyst served as the working electrode. On the CH instrument software, the chronopotentiometry experiment was used and the software settings applied were as follows: the cathodic current applied is 0 mA, the time for cathodic current is 0 s, the anodic current is 10 mA, and time for anodic current is 6 hours. The potential limit is set at ±5 V, and the current switching priority is time-dependent. The current, time of charge flow, and volume of the gas obtained from the experiment are used with the equation, f = 4Fn/Q to calculate the Faradaic efficiency. Where f is the faradaic efficiency (%), F is the Faraday's constant (96,485 C mol^{-1}), n is the amount (mol) of O_2 gas evolved, and Q is the total charge passed during electrolysis.

In-situ Raman Measurements

The in-situ Raman measurements were obtained using two different lasers. The first setup was done by drop-casting 24 µL (3 µL × 8) on a gold substrate and assembled in a 3D-printed cell[45,46] using 1 M KOH electrolyte, and the reference and counter electrode are Hg/HgO (1 M KOH) and graphite, respectively. Renishaw inVia Raman system, comprising an Ar-ion laser (514 nm, 50 mW), supplies an excitation beam, which is focused onto the sample via a 50× objective lens microscope. The laser was stationed above the working electrode and covered with a polymer film to avoid contact with the electrolyte. The Spectro-electrochemistry sequence was obtained in the spectrum range between 200 and 2000 cm^{-1}, and the laser exposure time was 30 s. First, the spectroelectrochemistry was obtained at the open circuit potential, and then subsequent electrochemistry was simultaneously obtained using chronoamperometry at potentials between 1.0-1.6 V vs RHE for the same period.

In the second setup, a gold screen-printed electrode (SPE) was electrochemically roughened by covering the surface of the working electrode with 0.1 M KCl (~100 µL) followed by thirty CV scans. The in-situ surface-enhanced Raman (SERS) measurements were obtained by drop-casting 5 µL (1 µL × 5) of the precatalyst on the Au SPE and assembled in a 3D-printed cell using 1 M KOH electrolyte, and the reference and counter electrode are Hg/HgO (1 M KOH) and nickel foam (2 × 2cm^2), respectively.[47] Horiba LabRAM ARAMIS confocal Raman microscope system, comprising of a He-Ne laser (633 nm, 50 mW) supplies an excitation beam focused on the sample via a 50× objective lens microscope. The laser was stationed above the electrochemical cell with a polymer film window to avoid contact with the electrolyte. The Spectro-electrochemistry sequence was obtained in the spectrum range between 200 and 2000 cm^{-1} and the laser exposure time was 30 s. First, the Spectro electrochemistry was obtained at the open circuit potential, and then subsequent electrochemistry was simultaneously obtained using chronoamperometry at potentials between 1.0-1.6 V vs RHE for the same period.

ICP-MS Measurements

The variants of the Ce_xNi_{1-x}-NMOF were digested by first weighing 2.5 mg of the samples and dissolving them in 1 mL of Aqua regia. The samples were digested and heated to dryness at 108 °C for 1 hour using a 5 mL conical interior Savillex vial, after which the samples were allowed to cool. After drying, the samples were reconstituted with 3 mL of Aqua regia. All samples were diluted 37.5-fold using 2 % HNO_3 by mixing 267 µL of the samples in a total volume of 10 mL of 2 % HNO_3 for two reasons:

To keep the total dissolved solids below 200 ppm is a required safety precaution for the instrument.

To eliminate the matrix effect that may occur due to density differences between the digesting solvent (Aqua regia) and the calibration solvent (2 % HNO_3).

Next, the samples were diluted further to keep Ce at concentrations < 200 ppb, which is the maximum calibration standard used for rare earth metals. This was completed by dissolving 15 µL of the previous diluent in 10 mL of 2 % HNO_3.

Microcrystal Electron Diffraction (MicroED)

Microcrystal electron diffraction (MicroED) data was collected as described by Jones et al.[48] Powders of Ce_0Ni_1-NMOF and $Ce_{0.03}Ni_{0.97}$-NMOF were ground lightly between glass microscope slides and transferred to carbon copper TEM grids. Diffraction data were measured using a ThermoFisher Glacios cryogenic transmission electron microscope (TEM) at a temperature of 100 K and an accelerating voltage of 200 kV

View Article Online
DOI: 10.1039/D5TA09289B

(0.0251 Å). The sample stage was continuously rotated from -60° to +60° at a rate of 1 ° s^{-1} and data were collected using the EPU-D data collection software; patterns were recorded on a Ceta-D camera optimized for low-dose diffraction. Crystals suitable for diffraction were sparse, and only one crystal from each sample batch yielded diffraction data suitable for indexing and subsequent structure solution. For Ce_0Ni_1-NMOF, this crystal diffracted to 0.65 Å and for $Ce_{0.03}Ni_{0.97}$-NMOF the crystal diffracted to 0.70 Å. Despite the low symmetry and incompleteness of the data, the relatively high resolution made structure solution possible.

Data reduction was performed using X-ray Detector Software (XDS).[49] Using Olex2 1.5,[50] the structure was solved via Intrinsic Phasing using SHELXT and refined by full-matrix least-squares on F^2 with anisotropic displacement parameters for the non-H atoms using the SHELXL[51] refinement package utilizing electron scattering factors.[52] Hydrogens were inserted using the HADD function and refined isotropically in idealized positions. The refinement of the occupancies of the O and N positions was guided by FTIR data collected from the samples. The occupancies were refined at ½ for N and O atoms in the Ce_0Ni_1-NMOF; while in the $Ce_{0.03}Ni_{0.97}$-NMOF, the occupancy of O is ¾ and the occupancy of N is 1.4. Restraints (RIGU 0.001, ISOR 0.005) on anisotropic displacement parameters were necessary Details of crystal data, data collection, and structure refinement are listed in Table S2.

Results and Discussion

Nitridation Temperature Optimization

The nickel-MOF (Ce_0Ni_1-MOF) was nitrided into Ce_xNi_{1-x}-NMOF employing a series of temperatures from 300-450 °C under NH_3 flow to obtain the optimum temperature needed for the formation of the Ni_3N phase. As shown in Figure S1, temperatures above 350 °C had metallic nickel with possibly reconstructed carbon fragments from the MOF as the dominant phase, which is due to an excessive reduction. However, at 350 °C, diffraction patterns match the formation of nickel nitride and a reconstructed carbon framework. This suggests that 350 °C is the optimum temperature needed for the desirable formation of the nitride phase.

Precursor to Precatalyst Characterization

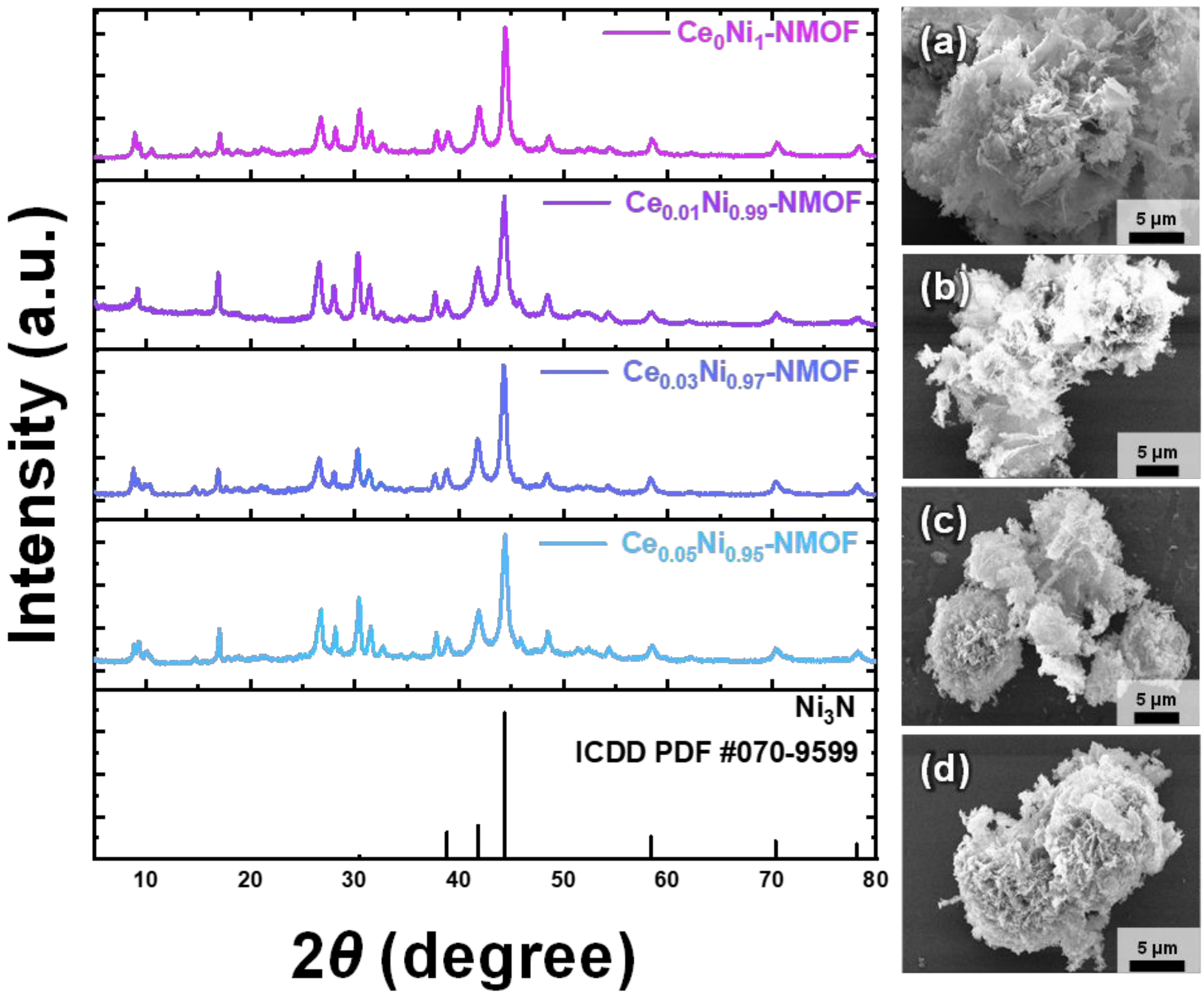

Figure 1: XRD and SEM images of pristine (a) Ce_0Ni_1-NMOF, (b) $Ce_{0.01}Ni_{0.99}$-NMOF, (c) $Ce_{0.03}Ni_{0.97}$-NMOF, and (d) $Ce_{0.05}Ni_{0.95}$-NMOFs. Ce-doping does not impact the bulk composite crystal and morphology.

View Article Online
DOI: 10.1039/D5TA09289B

The Ce_xNi_{1-x}MOFs and Ce_xNi_{1-x}NMOFs were characterized by powder X-ray diffraction (PXRD) to obtain crystallographic information about the samples. As displayed in Figure S2, all the samples shared diffraction patterns similar to the parent MOF-Ce_0Ni_1MOF's (CCDC #638866) [43], which meant that the Ce-doping didn't change the crystal structure, and this is very likely due to the low concentration. On the nitridation of the Ce_xNi_{1-x}MOFs, the as-obtained Ce_xNi_{1-x}NMOFs diffraction patterns as shown in Figure 1 were all similar, hence it can be inferred that the bulk of the sample were not impacted by Ce-doping even after nitridation. Next, we evaluated the morphology and chemical composition of the Ce_xNi_{1-x}NMOFs using SEM and EDX. SEM images in Figures 1 and S3-S5 reveal that all Ce_xNi_{1-x}-NMOFs exhibited a flower-like architecture with a mixed crystalline-amorphous and sheet-like morphology (see also in S23). EDX elemental mapping in Figures 2 and S3-S5 shows a homogenous distribution of the elements with the sparse spread of cerium in the bulk, as expected. Their corresponding EDX spectra in Figures S6, S7, and S8 also indicate the presence of the constituent elements in the bulk of all Ce_xNi_{1-x}-NMOFs samples.

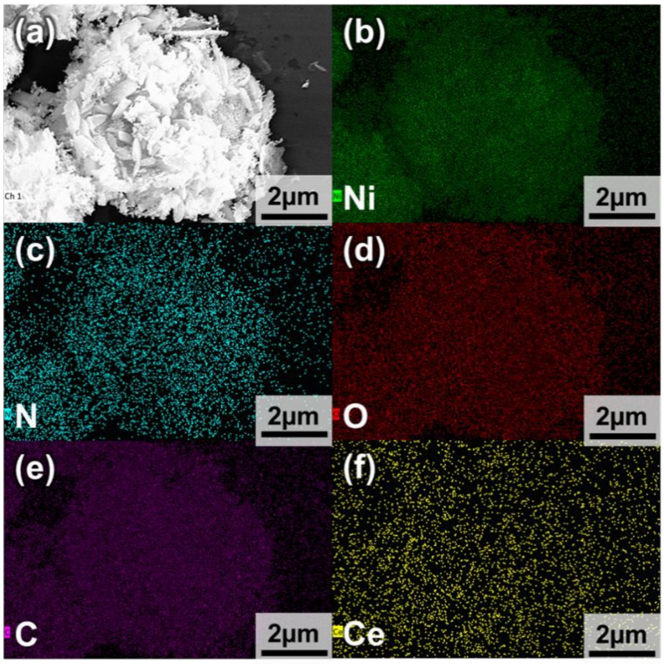

Figure 2: SEM and EDX elemental mapping images of $Ce_{0.03}Ni_{0.97}$-NMOF.

Next, we examined the Ce_xNi_{1-x}MOFs and the Ce_xNi_{1-x}NMOFs using X-ray photoelectron spectroscopy (XPS) to determine the chemical speciation on the surface. High-resolution spectra in Figure S9 show that the pristine Ce_xNi_{1-x}MOFs comprise Ce 3d, Ni 2p, O 1s, and C 1s core levels on the surface. All the elements in the sample sets were charge-corrected with a C 1s value of 284.8 eV. In Figure S9a, the peaks between 898 and 910 eV are due to Ce $3d_{3/2}$ spin-orbit coupling, and they show that Ce exist as predominantly Ce^{3+} species (904.0 eV) with Ce^{4+} species (899.9 and 906.7 eV) occurring due to surface oxidation.[53–55] In Figure 3a, although the Ce_xNi_{1-x}-NMOFs showed an increased mixture of Ce^{4+} and Ce^{3+} species with Ce-doping, there is an increase in the Ce^{3+} population compared to those of Ce_xNi_{1-x}MOFs that can be attributed to the reduction of Ce^{4+} species under a reducing environment ammonia ambient. The reduction starts with the thermal dissociation of ammonia into H_2 and NH_x radical ions, which interact with Ce^{4+} to release or extract oxygen, leading to the formation of oxygen vacancies and the byproduct Ce^{3+}.[56]

The Ni $2p_{3/2}$ band for Ce_xNi_{1-x}MOFs (Figure S9b) shows that Ni^{2+} (855.9 and 859.4 eV) species exist as Ni–O and Ni–OH which are the bonding environment between Ni and terephthalic acid (TPA).[57] The intensity of the Ni^{2+} peaks decreased and the binding energy shifted slightly to the right with increasing Ce content. In addition, the Ce^{3+} to $Ni^{>2+}$ charge transfer is evident in the increase of the Ce^{4+} population as confirmed in the Ce 3d spectra (see Figure S9a). Upon nitridation, the Ni band in Figure 3b indicates the binding energy shift to 852.6 from 855.0 eV (in Figure S9b), indicating the formation of Ni^0, which is direct evidence for the formation of the metallic nickel nitride phase,[58–60] corroborating the diffraction pattern in Figure 1. C 1s spectra in Figure 3c indicate the presence of the benzoic ring, carbonyl, and C–O groups from the TPA linkers at 284.8, 288.5, and 286.3 eV, respectively.[57] Core level spectra for O 1s in Figure 3d show a mix of Ni and Ce lattice hydroxides at 531.4, while 532.4 and 535.1 eV represent oxygen from the carbonyl groups and adsorbed water, respectively.[57,61] In Figure 3e, the N 1s spectra for all Ce_xNi_{1-x}NMOFs are shown. The binding energy at 398.1 eV and 399.6 eV indicates the presence of the lattice Ni–N bond,[58–60] and adsorbed NH_2[62] respectively for all the nitrided Ce-doped samples (black arrows). Ce_0Ni_1-NMOFs exhibited an oxidized surface chemistry as indicated by a shift in the binding energy from 398.1 eV (Ce-doped) to 398.7 eV and the adsorption of NH_x species at 400.3 eV.[58–60] These results indicate that nitirdation aids the formation of metallic nickel nitride.

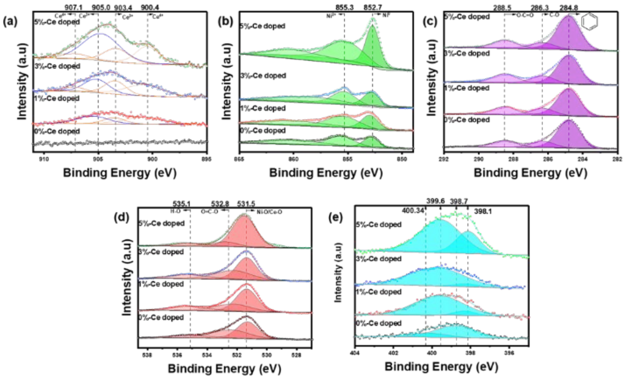

Figure 3: XPS spectra of Ce_xNi_{1-x}-NMOF showing (a) Ce 3d, (b) Ni 2p, (c) C 1s, (d) O 1s, and (e) N 1s.

Next, Ce_xNi_{1-x}MOFs and Ce_xNi_{1-x}NMOFs were characterized with FTIR to determine the functional group distribution in the samples. In the group frequency region as shown in Figure 4a, 1570 and 1375 cm^{-1} represent coordinated bi-dentate

View Article Online
DOI: 10.1039/D5TA09288B

vibrations modes from v_{asym}(COO) and vsym(COO) respectively from the TPA linker.[63–66] Additional vibrational modes between 3058 to 3427 cm^{-1} can be ascribed to strong OH from adsorbed water stretching while bands between 3587 to 3608 cm^{-1} express the presence of weak OH- stretching perhaps from remnant ethanol used in the washing process.[67,68] After nitridation, the as-synthesized Ce_xNi_{1-x}-NMOFs spectra in Figure 4b show that all the samples exhibited a red shift for the v_{asym}(COO) from 1570 to 1556.46 cm^{-1} which can be attributed to an attenuation or removal of some v_{asym}(COO) bond within the molecule by volatilization as CO_2 (g) or a stronger coordination of the v_{asym}(COO) to Ni centers. Conversely, the v_{sym}(COO) expressed a blue shift from 1375 to 1382 cm^{-1} which can be attributed to two factors. First, the availability of free v_{sym}(COO) due to the weakening or replacement of some of the v_{sym}(COO) coordinated to the Ni center with the Ni–N bond (not observed in IR). In addition, it can also be attributed to the coordination switch of v_{sym}(COO) from Ce to Ni after nitridation for the Ce-containing samples.

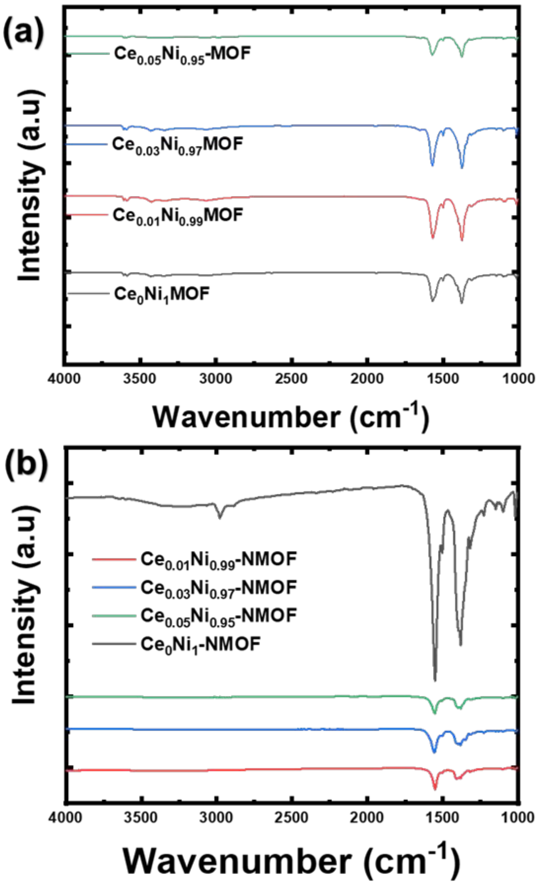

Figure 4: FTIR spectra showing functional groups vibrational bands in (a) Ce_xNi_{1-x}-MOF and (b) Ce_xNi_{1-x}-NMOF.

Intrinsic OER Activity

The electrochemical performance of the various precatalysts was evaluated to check for the effect of Ce-doping and nitridation. To understand the role of Ce-doping in electrocatalytic performance, the OER geometric activity was measured using CV as shown in Figure 5a. Results in Figure 5b indicate that the overpotentials of Ce_0Ni_1-NMOF, $Ce_{0.01}Ni_{0.99}$-NMOF, $Ce_{0.03}Ni_{0.97}$-NMOF, and $Ce_{0.05}Ni_{0.95}$-NMOF are 527 ± 31.64, 465 ± 16.80, 426 ± 12, and 528 ± 29.64 mV, respectively with $Ce_{0.03}Ni_{0.97}$-NMOF showing the lowest value. The Tafel slope was measured using steady-state multi-step chronopotentiometry (MUSCP) as indicated in Figure S10, and representative resultant Tafel plots are shown in Figure S11, while results from replicate measurements are also available in Figure 5b. The results demonstrate that the Tafel slope values were 114.32 ± 4.67, 97.74 ± 1.45, 83.6 ± 7.19, and 95.87 ± 3.33 mV dec^{-1} for Ce_0Ni_1-NMOF, $Ce_{0.01}Ni_{0.99}$-NMOF, $Ce_{0.03}Ni_{0.97}$-NMOF, and $Ce_{0.05}Ni_{0.95}$-NMOF, respectively. A similar trend was observed in the R_{ct} values measured using EIS (Figure S12, results in Figure 5b) measurements, where $Ce_{0.03}Ni_{0.97}$-NMOF has the lowest value of 37.6 ± 5.82 Ω. Clearly, the $Ce_{0.03}Ni_{0.97}$-NMOF had a better electrochemical performance compared to others. Catalytic performance was also assessed by measuring the double-layer capacitance (C_{dl}) using EIS and then normalized to a generic specific capacitance (Cs) of 40 µF cm^{-2} in an alkaline system to obtain the electrochemical surface area (ECSA).[69] The results in Figure S13a reveal that the $Ce_{0.03}Ni_{0.97}$-NMOF has one of the lowest ECSAs and the highest intrinsic activity as indicated by the current density normalized to the ECSA in Figure S13b. However, it was observed that at cerium concentrations >3%, the population of ceria (Ce^{4+}), which is a well-known insulator, accumulates on the surface as observed in Figure 3a and could likely increase under oxidizing reaction conditions. Next, we try to evaluate the stability of $Ce_{0.03}Ni_{0.97}$-NMOF using long-term CP, and the result shown in Figure 5c shows that the electrocatalyst is stable for at least 12 hours at a current density of 10 mA cm^{-2}. The observed decrease in the potential could be due to increasingly exposed active sites under the long-term OER potential, which lowered the energy requirement for the OER. It's also noteworthy that the electrochemical activity (inset of Figure 5c) still increases by ~ 25 mA cm^{-2} after long-term CP testing, demonstrating that the electrochemical performance improves even after 12 hours. We also conducted a 24-hour CP test, as shown in Figure S22, and $Ce_{0.03}Ni_{0.97}$-NMOF still maintains its stability. Post-long-term CP characterization by EDX, shown in Figure 6 (spectra in Figure S8), shows that $Ce_{0.03}Ni_{0.97}$-NMOF retains its Ni and O content. However, the C and N signals are convoluted by signals emerging from the carbon paper and the fumion ® binder, respectively. XPS spectra (shown in Figure S8) reveals that the N 1s peak at 398.1 eV diminishes significantly compared to the pristine $Ce_{0.03}Ni_{0.97}$-NMOF, which is an indication of the loss of lattice nitrogen.[59] In addition, the peak at ~403.5 eV, which was absent in the pristine sample, becomes prominent, which can be attributed to nitrogen contributions from Fumion® binder. Pristine and Post-OER electrolyte analysis (Table S1) using ICP-MS showed that Ce is not present in the electrolyte before the reaction neither was there any leaching of Ce from $Ce_{0.03}Ni_{0.97}$-NMOF which is also an indication of its electrochemical stability. To evaluate the kinetic regime governing $Ce_{0.03}Ni_{0.97}$-NMOF, a scan-rate dependent electrochemical analysis was conducted to

View Article Online
DOI: 10.1039/D5TA09289B

probe mass transport behavior. CV's were recorded at varying scan rates, and the relationship between peak current and scan rate was analyzed using the power-law expression ($i = av^b$).[70] A b-value of 0.74 was obtained. In electrochemical systems, a b-value of 0.5 corresponds to a diffusion-controlled process, whereas a value approaching 1.0 indicates a surface-controlled or capacitive process. The observed intermediate b-value of 0.74 suggests that the catalytic response is governed by a mixed mechanism, with contributions from both diffusion-limited mass transport and surface or pseudocapacitive charge-transfer processes.[70,71] This indicates that although ion diffusion within the electrolyte and porous catalyst framework influences the overall current response, a substantial fraction of the current originates from rapid interfacial redox reactions occurring at accessible active sites. Overall, the results demonstrate partial mitigation of diffusion limitations and enhanced surface reactivity, consistent with improved electrochemical performance.

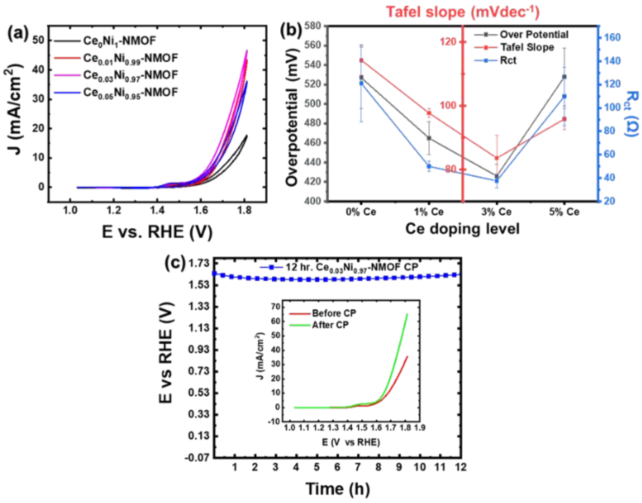

Figure 5: (a) CV showing impact of Ce doping on electrochemical activity (b) Effect of Ce-doping on electrochemical metrics (c) CP plot showing electrochemical stability of $Ce_{0.03}Ni_{0.97}$-NMOF with inset showing linear sweep voltammetry curves indicating activity.

Next, to show that nitridation played an active role in the OER activity, we compared the electrochemical activity of the best-performing precatalyst $Ce_{0.03}Ni_{0.97}$-NMOF with its MOF counterpart, $Ce_{0.03}Ni_{0.97}$-MOF. As shown in Figure S14, nitrogen incorporation into the lattice structure of the MOF improved its electrochemical activity by more than a factor of approximately 50. This re-emphasizes the role of nitrogen incorporation into the crystal lattice of MOFs in that it augments electron transfer thereby aiding electrochemical activity.[72]

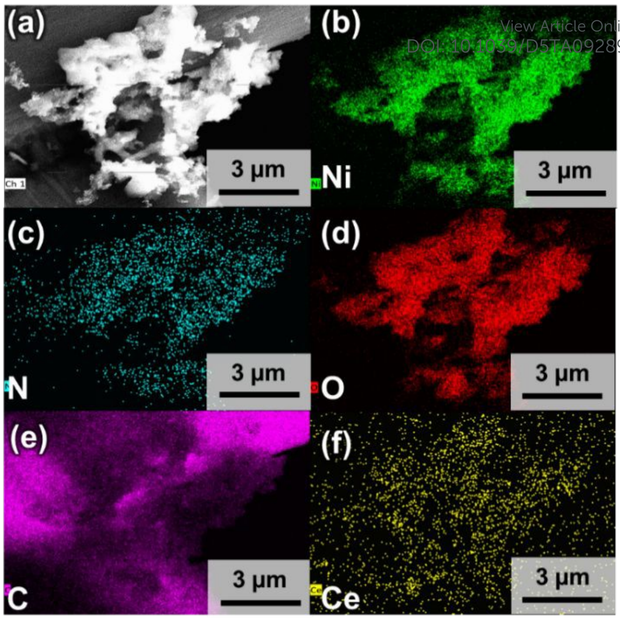

Figure 6: Post-OER SEM and EDX elemental mapping images of $Ce_{0.03}Ni_{0.97}$-NMOF.

Structural Contributions to Improved OER Activity

With PXRD unable to discern between the Ce-doped and undoped nitride samples, in the next step, we employed the more precise microcrystal electron diffraction (MicroED) method to obtain the structure of the synthesized $CexNi_{1-x}$-NMOF to delineate a structural explanation for the electrochemical activity. MicroED is uniquely beneficial for the structural interrogation of micro-crystalline samples in the absence of large crystals required for conventional single-crystal XRD analysis. The crystal structure solved by MicroED (Figure S15a) shows that Ce_0Ni_1-NMOF possesses a linear or 1D structure. It does not contain Ce as expected, and Ni resides in a pseudo-octahedral sphere coordinated with oxygen atoms from the benzoic acid functionality of TPA, in accordance with FTIR results. The nitrogen atoms are also observed to be bonded to the Ni atom in the chemical structure of Ce_0Ni_1-NMOF which supports the XRD results. Surprisingly, the crystal structure of $Ce_{0.03}Ni_{0.97}$-NMOF (Figure S15b) does not indicate the presence of Ce. The absence of Ce in $Ce_{0.03}Ni_{0.97}$-NMOF could be due to its absence in the bulk due to its low concentration which makes it below the detection limit for the MicroED. However, because the cerium contents are on the surface, rather than in the bulk, they can be detected with XPS. Also, Ce exist in the amorphous phase, which is also a condition at which MicroED cannot resolve structures. The Ni atoms exist in unique pseudo-octahedral and pseudo-tetrahedral geometries, coordinated by oxygen atoms from TPA as predicted by FTIR or from nitrogen atoms as predicted by XRD. Oxygen is resolved to possess a 75% occupancy due to its predominant fingerprint from other characterization techniques such as XPS and FTIR while nitrogen is resolved to have a 25% occupancy since C=N or C-N weren't observed in FTIR perhaps due to a lower abundance. The pseudotetrahedral geometry on Ni (opposed to the octahedral geometry) can be ascribed to oxygen removal by cerium doping.

View Article Online
DOI: 10.1039/D5TA09289B

The chemical structure of $Ce_{0.03}Ni_{0.97}$-NMOF suggests that the pseudo-tetrahedral geometry on Ni leave room for the adsorption of OH* adsorbates thereby facilitating OER compared to Ce_0Ni_1-NMOF.[7,39–42] It is well reported that Ce has a high affinity for oxygen atoms, as marked by a higher bond dissociation energy of 795 kJ mol^{-1} compared to Ni (391 kJ mol^{-1}),[73] and this may lead to structural evolution near the Ni.[74] It is also possible that Ce-doping disrupts the neighboring Ni–O bond formation and, coupled with carboxylate recoupling leads to the growth of $Ce_{0.03}Ni_{0.97}$-NMOF in the periodic 3D lattice. To provide evidence for the location/presence of Ce and nitride species in the precatalyst, we obtained TEM images and elemental mapping. Elemental mapping of Ce_0Ni_1-NMOF in Figure S16 shows the spatial distribution of the expected elements, most importantly nitrogen confirming the presence of the nitride species which is supported by the corresponding spectra in Figure S18a indicating the clear absence of Ce and the detection of nitrogen as expected. The presence of Ce and nitrogen in $Ce_{0.03}Ni_{0.97}$-NMOF is also confirmed by the elemental mapping in Figure S17 which is supported by the spectra in Figure S18b. Nonetheless, ICP-MS further confirmed the presence of Ce in the various Ce-doped samples and checked that the Ce:Ni ratio is as-synthesized as shown in Table S1.

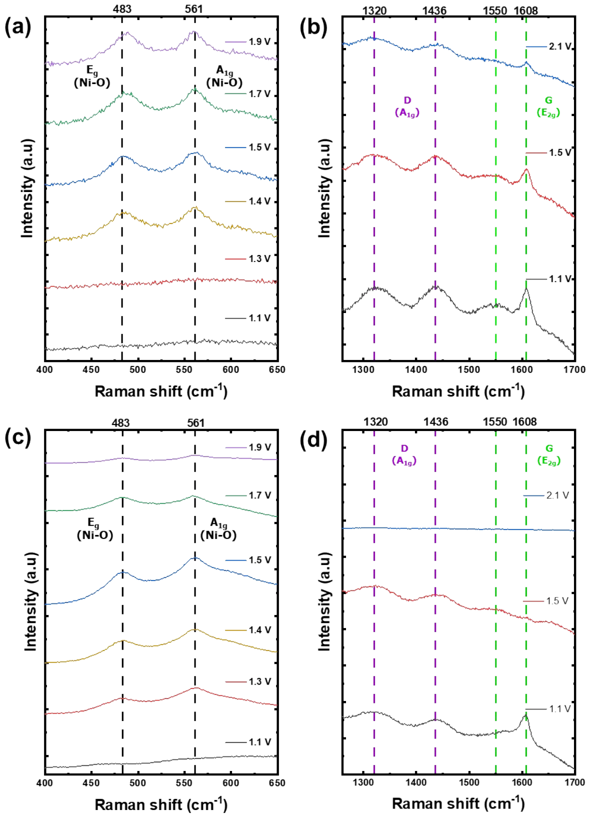

Figure 7: In-situ surface-enhanced Raman measurements (633 nm) at various potentials showing (a) NiOOH and (b) graphitic carbon bands in Ce_0Ni_1-NMOF and (c) NiOOH and (d) graphitic carbon bands in $Ce_{0.03}Ni_{0.97}$-NMOF.

In-situ Raman measurements were obtained to observe characteristic vibration modes of the active phases during landmark OER events and potentials for Ce_0Ni_1-NMOF and $Ce_{0.03}Ni_{0.97}$-NMOF. This was done to identify the catalytic OER active phases and provide more insight into the role of Ce-doping during the OER. As shown in Figure 7a, at potentials ≤1.3 V vs RHE, Raman bands of Ce_0Ni_1-NMOF at 483 and 561 cm^{-1} which are Ni–O signature bands in NiOOH[75,76] were absent, while in Figure 7b, peaks observed at 1320-1436 and 1550-1608 cm^{-1}, were observed which are indicative of the D (A_{1g} mode) and G (E_{2g} mode) graphitic carbon bands, respectively.[77,78] This suggests that prior to OER onset potentials (≤ 1.3 V vs RHE), the graphitic carbon frameworks are present which has been confirmed by other characterization techniques; and the nickel-nitride sites are yet to be oxidized sufficiently to generate the Ni–O bond in NiOOH. In addition, since the D band typically represents defects in a carbon framework while the G bands represent sp^2 in-plane vibrational modes, the relatively smaller intensity of the G-band compared to the D-band provides evidence that there are more structural defects in the carbon framework than an ordered carbon ring structure below OER potentials.[79] However, at OER overpotentials, specifically 1.40 V vs RHE, the twin Ni^{3+}–O modes at 483 and 561 cm^{-1} are observed, indicating an oxidation of the Ni_3N to NiOOH. Previous studies have shown that at Raman shifts of 483 and 561 cm^{-1}, NiOOH can be identified as β-NiOOH type and when the peaks heights. [80] In addition, as the potentials increase from 1.1 to 2.1 V vs RHE, there is a gradual diminishing of the carbon bands. Two possible reasons for the peak disappearance could be OER conditions or the beam energy.[81,82] To check to see which of the aforementioned reasons is the key player, we interrogated the surface in an ex-situ setup. After the ex-situ interrogation of the precatalyst, the emergence of the graphitic framework was observed as shown in Figure S19. The resulting evidence suggests that some of the graphitic carbon structure was preserved even after the OER, and the absence of the graphitic carbon framework can be due to beam damage due to prolonged exposure. Another experiment was conducted with a high energy beam of 514 nm and as shown in Figures S20a and b, the Ni-O peaks at 477-560 cm^{-1} and the carbon bands at 1381-1606 cm^{-1} were diminished indicating the role of beam intensity on observed Raman features. In Figures 7c and d, a similar observation in Ce_0Ni_1-NMOF is noted in $Ce_{0.03}Ni_{0.97}$-NMOF Raman bands. Unlike Ce_0Ni_1-NMOF, there is an early development of the β-NiOOH peak at 1.3 V for $Ce_{0.03}Ni_{0.97}$-NMOF that wasn't observed in Ce_0Ni_1-NMOF which suggests that incorporation of Ce induces the early formation of the active site that facilitates OER activity by generating the highly active CeO_2-NiOOH due to the formation of the pseudo-tetrahedral structure as suggested by the MicroED. At potentials ≥ 1.3 V vs RHE, where OER currents are observed, the twin peak of β-NiOOH emerges as the dominant active site in that regime. Also, the graphitic carbon framework completely disappears as observed in Figure 7d at 2.1V, but is observed even in the ex-situ setup after the OER reaction (Figure S19) with the D bands having a higher intensity compared to the

View Article Online
DOI: 10.1039/D5TA09289B

pristine material, indicative of an increased disorder in the graphitic carbon framework. The faster decrease in the intensity of the carbon bands in $Ce_{0.03}Ni_{0.97}$-NMOF compared to Ce_0Ni_1-NMOF in the in-situ setup can additionally be due to higher activity of the former compared to the latter.

Conclusions

We outlined a synthetic method that utilizes nitridation and Ce-doping in transforming a non-conductive Ni-based MOF into a conductive precatalyst suitable for driving the OER in alkaline media. Nitridation modified the chemical environment and electronic properties of the parent MOF while Ce-doping possibly aided the formation of pseudo-tetrahedral geometry on Ni sites which likely impacted the binding energy of the adsorbates leading to improved intrinsic activity. By applying different temperature regimes, we optimized the nitridation process which yielded metallic Ni^0 and Ce^{3+} as the metallic centers and a flower-like carbon framework. Electrochemical data reveals that of all the various Ce-doped precatalysts, $Ce_{0.03}Ni_{0.97}$-NMOF had the best OER performance as marked by the highest intrinsic activity, lowest charge transfer resistance, and Tafel slope. Further evaluation revealed that $Ce_{0.03}Ni_{0.97}$-NMOF was stable for 12 hours at a current density of 10 mA cm^{-2} and even demonstrated electrochemical activity improvement afterward. With MicroED, the pseudo-tetrahedral geometry on Ni sites was structurally observed, and in-situ Raman measurement revealed that this geometry induces an early formation of β-NiOOH, which is also an OER active phase responsible for improved electrochemical metrics. Overall, the results show that nitridation and Ce-doping produced a precatalyst with an augmented activity and stability relative to the parent Ni-based MOF.

Author contributions

C. E. Chukwuneke: conceptualization, investigation, methodology, formal analysis, writing– original draft, visualization. **K. Kawashima**: conceptualization, investigation, methodology, formal analysis, writing-review and editing, visualization. **T. P. A Nguyen**: Investigation. **G. Ruiz**: investigation, writing, formal analysis. **JP. Smith**: Investigation. **R. A. Márquez**: investigation, writing – review & editing. **J. T. Bender**: investigation, writing – review & editing. **X. Zhan**: Investigation. **D. J. Milliron**: writing – review & editing, resources. **M. J. Rose**: writing – review & editing, resources. **C. B. Mullins**: writing – review & editing, resources, funding acquisition, project administration.

Conflicts of interest

There are no conflicts to declare.

Acknowledgements

The authors gratefully acknowledge the support of the National Science Foundation (NSF) via Grant CHE-2102307 and for the acquisition of the VersaProbe-IV XPS supported by the NSF Major Research Instrumentation program (Grant MRI-2117623). This project was also supported by the Allen J. Bard Center for Electrochemistry Welch Grant "Welch Foundation H-F-0037", grant supporting MJR/GNR "Welch Foundation grants F-1822 and X-F-0003-20230731", and the Welch grant number (F-1848). MicroED data were collected at the Sauer Structural Biology Lab at the University of Texas at Austin.

References

1 N. Stock and S. Biswas, *Chem. Rev.*, 2012, **112**, 933–969.

2 A. Mahmood, W. Guo, H. Tabassum and R. Zou, *Advanced Energy Materials*, 2016, **6**, 1600423.

3 W. Zheng and L. Y. S. Lee, *ACS Energy Lett.*, 2021, **6**, 2838–2843.

4 W. Zheng, M. Liu and L. Y. S. Lee, *ACS Catal.*, 2020, **10**, 81–92.

5 K. Kawashima, R. A. Márquez, L. A. Smith, R. R. Vaidyula, O. A. Carrasco-Jaim, Z. Wang, Y. J. Son, C. L. Cao and C. B. Mullins, *Chem. Rev.*, 2023, **123**, 12795–13208.

6 O. Mabayoje, A. Shoola, B. R. Wygant and C. B. Mullins, *ACS Energy Lett.*, 2016, **1**, 195–201.

7 B. R. Wygant, K. Kawashima and C. B. Mullins, *ACS Energy Lett.*, 2018, **3**, 2956–2966.

8 S. Jin, *ACS Energy Lett.*, 2019, **4**, 1443–1445.

9 Y. Li, B. Jia, Y. Fan, K. Zhu, G. Li and C.-Y. Su, *Advanced Energy Materials*, 2018, **8**, 1702048.

10 T. Wang, Z. Kou, S. Mu, J. Liu, D. He, I. S. Amiinu, W. Meng, K. Zhou, Z. Luo, S. Chaemchuen and F. Verpoort, *Advanced Functional Materials*, 2018, **28**, 1705048.

11 Z. Wang, Y. Lu, Y. Yan, T. Y. P. Larissa, X. Zhang, D. Wuu, H. Zhang, Y. Yang and X. Wang, *Nano Energy*, 2016, **30**, 368–378.

12 B. Y. Xia, Y. Yan, N. Li, H. B. Wu, X. W. (David) Lou and X. Wang, *Nat Energy*, 2016, **1**, 1–8.

13 F. Yang, P. Zhao, X. Hua, W. Luo, G. Cheng, W. Xing and S. Chen, *J. Mater. Chem. A*, 2016, **4**, 16057–16063.

14 Y.-N. Chen, Y. Guo, H. Cui, Z. Xie, X. Zhang, J. Wei and Z. Zhou, *J. Mater. Chem. A*, 2018, **6**, 9716–9722.

15 B. Chen, X. He, F. Yin, H. Wang, D.-J. Liu, R. Shi, J. Chen and H. Yin, *Advanced Functional Materials*, 2017, **27**, 1700795.

View Article Online
DOI: 10.1039/D5TA09289B

16 L. Wei, H. E. Karahan, S. Zhai, H. Liu, X. Chen, Z. Zhou, Y. Lei, Z. Liu and Y. Chen, *Advanced Materials*, 2017, **29**, 1701410.

17 J. Qian, T.-T. Li, Y. Hu and S. Huang, *Chem. Commun.*, 2017, **53**, 13027–13030.

18 J. Jiang, C. Zhang and L. Ai, *Electrochimica Acta*, 2016, **208**, 17–24.

19 X. Dong, E. Yan, Y. Lv, Y. Zhou and X. Chu, *Applied Catalysis A: General*, 2024, **681**, 119772.

20 S. Anantharaj, S. R. Ede, K. Sakthikumar, K. Karthick, S. Mishra and S. Kundu, *ACS Catal.*, 2016, **6**, 8069–8097.

21 F. Ming, H. Liang, H. Shi, X. Xu, G. Mei and Z. Wang, *J. Mater. Chem. A*, 2016, **4**, 15148–15155.

22 S. Li, S. Peng, L. Huang, X. Cui, A. M. Al-Enizi and G. Zheng, *ACS Appl. Mater. Interfaces*, 2016, **8**, 20534–20539.

23 Q. Dong, Q. Wang, Z. Dai, H. Qiu and X. Dong, *ACS Appl. Mater. Interfaces*, 2016, **8**, 26902–26907.

24 X. Liu, Y. Liu and L.-Z. Fan, *J. Mater. Chem. A*, 2017, **5**, 15310–15314.

25 Y. Guo, J. Tang, Z. Wang, Y.-M. Kang, Y. Bando and Y. Yamauchi, *Nano Energy*, 2018, **47**, 494–502.

26 L.-L. Wu, Q.-S. Wang, J. Li, Y. Long, Y. Liu, S.-Y. Song and H.-J. Zhang, *Small*, 2018, **14**, 1704035.

27 X. Zhang, S. Liu, Y. Zang, R. Liu, G. Liu, G. Wang, Y. Zhang, H. Zhang and H. Zhao, *Nano Energy*, 2016, **30**, 93–102.

28 S. Liu, X. Zhang, G. Wang, Y. Zhang and H. Zhang, *ACS Appl. Mater. Interfaces*, 2017, **9**, 34269–34278.

29 Y. Guo, J. Tang, H. Qian, Z. Wang and Y. Yamauchi, *Chem. Mater.*, 2017, **29**, 5566–5573.

30 M. K. Aslam, S. S. A. Shah, S. Li and C. Chen, *J. Mater. Chem. A*, 2018, **6**, 14083–14090.

31 X.-Y. Yu, Y. Feng, B. Guan, X. W. (David) Lou and U. Paik, *Energy Environ. Sci.*, 2016, **9**, 1246–1250.

32 P. Wang, Z. Xu, Y. Lin, L. Wan and B. Wang, *ACS Sustainable Chem. Eng.*, 2020, **8**, 8949–8957.

33 X. Xiao, C.-T. He, S. Zhao, J. Li, W. Lin, Z. Yuan, Q. Zhang, S. Wang, L. Dai and D. Yu, *Energy Environ. Sci.*, 2017, **10**, 893–899.

34 J. Song, C. Zhu, B. Z. Xu, S. Fu, M. H. Engelhard, R. Ye, D. Du, S. P. Beckman and Y. Lin, *Advanced Energy Materials*, 2017, **7**, 1601555.

35 B. You, N. Jiang, M. Sheng, S. Gul, J. Yano and Y. Sun, *Chem. Mater.*, 2015, **27**, 7636–7642.

36 C. Guan, W. Xiao, H. Wu, X. Liu, W. Zang, H. Zhang, J. Ding, Y. P. Feng, S. J. Pennycook and J. Wang, *Nano Energy*, 2018, **48**, 73–80.

37 E. Hu, J. Ning, D. Zhao, C. Xu, Y. Lin, Y. Zhong, Z. Zhang, Y. Wang and Y. Hu, *Small*, 2018, **14**, 1704233.

38 S. Hu, S. Wang, C. Feng, H. Wu, J. Zhang and H. Mei, *ACS Sustainable Chem. Eng.*, 2020, **8**, 7414–7422.

39 K. Chen, R. Rajendiran, C. Deviprasath, S. Mathew, Y.-R. Cho, K. Prabakar and O. Lun Li, *ChemElectroChem*, 2022, **9**, e202200093.

40 S. Peng, F. Gong, L. Li, D. Yu, D. Ji, T. Zhang, Z. Hu, Z. Zhang, S. Chou, Y. Du and S. Ramakrishna, *J. Am. Chem. Soc.*, 2018, **140**, 13644–13653.

41 H. Xu, J. Cao, C. Shan, B. Wang, P. Xi, W. Liu and Y. Tang, *Angewandte Chemie*, 2018, **130**, 8790–8794.

42 L. Zhuang, L. Ge, Y. Yang, M. Li, Y. Jia, X. Yao and Z. Zhu, *Advanced Materials*, 2017, **29**, 1606793.

43 Y. Yan, P. Gu, S. Zheng, M. Zheng, H. Pang and H. Xue, *J. Mater. Chem. A*, 2016, **4**, 19078–19085.

44 K. Kawashima, R. A. Márquez, Y. J. Son, C. Guo, R. R. Vaidyula, L. A. Smith, C. E. Chukwuneke and C. B. Mullins, *ACS Catal.*, 2023, **13**, 1893–1898.

45 K. Kawashima, Y. J. Son, Z. Wang, R. F. Rose, R. A. Marquez-Montes, L. A. Smith, C. E. Chukwuneke and C. B. Mullins, *Meet. Abstr.*, 2023, **MA2023-02**, 3126.

46 A. E. F. Milton, K. Kawashima, Y. J. Son, W. J. Chang, Z. Wang, R. A. Marquez, R. F. Rose, D. J. Milliron and C. B. Mullins, *Meet. Abstr.*, 2024, **MA2024-02**, 4742.

47 R. A. Marquez, E. Kalokowski, M. Espinosa, J. T. Bender, Y. J. Son, K. Kawashima, C. E. Chukwuneke, L. A. Smith, H. Celio, A. Dolocan, X. Zhan, N. Miller, D. J. Milliron, J. Resasco and C. B. Mullins, *Energy Environ. Sci.*, 2024, **17**, 2028–2045.

48 C. G. Jones, M. W. Martynowycz, J. Hattne, T. J. Fulton, B. M. Stoltz, J. A. Rodriguez, H. M. Nelson and T. Gonen, *ACS Cent. Sci.*, 2018, **4**, 1587–1592.

49 W. Kabsch, *Acta Cryst D*, 2010, **66**, 125–132.

50 O. V. Dolomanov, L. J. Bourhis, R. J. Gildea, J. a. K. Howard and H. Puschmann, *J Appl Cryst*, 2009, **42**, 339–341.

51 G. M. Sheldrick, *Acta Cryst A*, 2008, **64**, 112–122.

52 L.-M. Peng, *Micron*, 1999, **30**, 625–648.

53 Aashima, S. Uppal, A. Arora, S. Gautam, S. Singh, R. J. Choudhary and S. K. Mehta, *RSC Adv.*, 2019, **9**, 23129–23141.

54 B. Shen, F. Wang and T. Liu, *Powder Technology*, 2014, **253**, 152–157.

55 M. Liu, K.-A. Min, B. Han and L. Y. S. Lee, *Advanced Energy Materials*, 2021, **11**, 2101281.

56 Y. Zhou, S. Ren, J. Yang, W. Liu, Z. Su, Z. Chen, M. Wang and L. Chen, *Journal of the Energy Institute*, 2021, **98**, 199–205.

57 F. Sun, G. Wang, Y. Ding, C. Wang, B. Yuan and Y. Lin, *Advanced Energy Materials*, 2018, **8**, 1800584.

58 C. E. Chukwuneke, K. Kawashima, H. Li, R. A. Marquez, Y. Jun Son, L. A. Smith, H. Celio, G. Henkelman and C. Buddie Mullins, *Journal of Materials Chemistry A*, 2024, **12**, 1654–1661.

59 K. Kawashima, R. A. Márquez-Montes, H. Li, K. Shin, C. L. Cao, K. M. Vo, Y. J. Son, B. R. Wygant, A. Chunangad, D. H. Youn, G. Henkelman, V. H. Ramos-Sánchez and C. B. Mullins, *Mater. Adv.*, 2021, **2**, 2299–2309.

60 M. Shalom, D. Ressnig, X. Yang, G. Clavel, T. Patrick Fellinger and M. Antonietti, *Journal of Materials Chemistry A*, 2015, **3**, 8171–8177.

61 J. Liu, Y. Liu, X. Mu, H. Jang, Z. Lei, S. Jiao, P. Yan, M. G. Kim and R. Cao, *Advanced Functional Materials*, 2022, **32**, 2204086.

62 K. Kawashima, M. Hojamberdiev, H. Wagata, K. Yubuta, K. Domen and K. Teshima, *ACS Sustainable Chem. Eng.*, 2017, **5**, 232–240.

63 N. P. Dileep, J. Patel and Y. Pushkar, *Inorg. Chem.*, 2024, **63**, 8050–8058.

64 Y. Zhu, Z. Chen, H. Li, Q. Wang, X. Liu, Y. Hu, C. Su, R. Duan, S. Chen and L. Lan, *Sci Rep*, 2023, **13**, 3386.

65 M. Lammert, C. Glißmann, H. Reinsch and N. Stock, *Crystal Growth & Design*, 2017, **17**, 1125–1131.

66 K. Tan, N. Nijem, P. Canepa, Q. Gong, J. Li, T. Thonhauser and Y. J. Chabal, *Chem. Mater.*, 2012, **24**, 3153–3167.

67 F.-L. Li, P. Wang, X. Huang, D. J. Young, H.-F. Wang, P. Braunstein and J.-P. Lang, *Angewandte Chemie*, 2019, **131**, 7125–7130.

68 Infrared Spectroscopy Absorption Table, https://chem.libretexts.org/Ancillary_Materials/Reference/Reference_Tables/Spectroscopic_Reference_Tables/Infrared_Spectroscopy_Absorption_Table, (accessed September 22, 2024).

69 C. C. L. McCrory, S. Jung, I. M. Ferrer, S. M. Chatman, J. C. Peters and T. F. Jaramillo, *J. Am. Chem. Soc.*, 2015, **137**, 4347–4357.

70 A. J. Bard, L. R. Faulkner and H. S. White, *Electrochemical Methods: Fundamentals and Applications*, John Wiley & Sons, 2022.

71 C. C. L. McCrory, S. Jung, J. C. Peters and T. F. Jaramillo, *J. Am. Chem. Soc.*, 2013, **135**, 16977–16987.

72 R. Jamil, R. Ali, S. Loomba, J. Xian, M. Yousaf, K. Khan, B. Shabbir, C. F. McConville, A. Mahmood and N. Mahmood, *Chem Catalysis*, 2021, **1**, 802–854.

73 T. L. Cottrell, *The strengths of chemical bonds*, London: Butterworths, 2nd edition., 1958.

74 Z. Huang, X. Liao, W. Zhang, J. Hu and Q. Gao, *ACS Catal.*, 2022, **12**, 13951–13960.

75 A. C. Garcia, T. Touzalin, C. Nieuwland, N. Perini and M. T. M. Koper, *Angewandte Chemie International Edition*, 2019, **58**, 12999–13003.

76 S. Lee, K. Banjac, M. Lingenfelder and X. Hu, *Angewandte Chemie International Edition*, 2019, **58**, 10295–10299.

77 C. Gu, H. Zhang, X. Wang and J. Tu, *RSC Adv.*, 2013, **3**, 11807–11815.

78 J. Guerrero-Contreras and F. Caballero-Briones, *Materials Chemistry and Physics*, 2015, **153**, 209–220.

79 A. C. Ferrari and J. Robertson, *Phys. Rev. B*, 2001, **64**, 075414.

80 Y. L. Lo and B. J. Hwang, *Langmuir*, 1998, **14**, 944–950.

81 L. A. Smith, K. Kawashima, R. A. Marquez and C. B. Mullins, *ACS Materials Lett.*, 2024, **6**, 3190–3201.

82 W. Zheng, *Chemistry–Methods*, **n/a**, e202200042.

View Article Online
DOI: 10.1039/D5TA09289B

All data is available in the manuscript and supporting information files.